

Microbubble implosions in finite hollow spheres

Cite as: Phys. Plasmas **29**, 013105 (2022); <https://doi.org/10.1063/5.0068815>

Submitted: 27 August 2021 • Accepted: 17 December 2021 • Published Online: 10 January 2022

 M. A. H. Zosa and  M. Murakami



View Online



Export Citation



CrossMark

Physics of Plasmas
Papers from 62nd Annual Meeting of the
APS Division of Plasma Physics

Read now!

Microbubble implosions in finite hollow spheres

Cite as: Phys. Plasmas **29**, 013105 (2022); doi: 10.1063/5.0068815

Submitted: 27 August 2021 · Accepted: 17 December 2021 ·

Published Online: 10 January 2022



M. A. H. Zosa^{1,2} and M. Murakami^{1,a)}

AFFILIATIONS

¹Institute of Laser Engineering, Osaka University, 2-6 Yamadaoka, Suita, Osaka 565-0871, Japan

²Division of Electrical, Electronic and Infocommunications Engineering, Graduate School of Engineering, Osaka University, 2-1 Yamadaoka, Suita, Osaka 565-0871, Japan

^{a)}Author to whom correspondence should be addressed: murakami-m@ile.osaka-u.ac.jp

ABSTRACT

Microbubble implosion (MBI) is a recently proposed novel mechanism with many interesting and exciting potential applications. MBI predicts that the inner layers of a spherical target with a hollow cavity can be compressed into a core with a density 10^5 times that of the solid density. Furthermore, this ultra-compressed core mostly consists of ions. This leads to the generation of ultra-high electric fields, which may be applicable to gamma-ray lensing or pair creation. However, MBI has yet to be studied for finite hollow spheres whose electrons are free to redistribute themselves after being given an initial temperature. This paper studies MBI under finite sphere conditions. Using an electron distribution model, the electron distribution after receiving an initial temperature is studied. Then, the optimal parameters required to fill a hollow cavity with electrons are calculated. The dynamics of MBI is simulated using a hybrid one-dimensional code. The simulation demonstrates that MBI occurs even for finite spheres, and high-density compression is still achievable with this setup. It also shows the optimal target structure, which maximizes ion flashing.

Published under an exclusive license by AIP Publishing. <https://doi.org/10.1063/5.0068815>

I. INTRODUCTION

The emergence of relativistic laser facilities^{1–4} ($>10^{18}$ W/m²) is a crucial factor in facilitating experiments involving various physical phenomena, such as ion acceleration,^{5–13} relativistic electron acceleration,^{14–18} nuclear fusion,^{19–23} or even quantum electrodynamics (QED).^{24–30} A more recent proposition which takes advantage of relativistic laser intensities is microbubble implosion (MBI).^{31,32} MBI is a new and exciting proposition because it has various scientific and technological applications, such as ion acceleration,³² gamma-ray lensing,³³ and even pair creation.³⁴

In MBI, a target with a spherical cavity is irradiated by an intense laser which heats the electrons. Once the electrons are heated, they start to fill the cavity and initiate the implosion of ions close to the cavity walls. The rapid implosion in MBI bears a similarity to another interesting phenomenon called sonoluminescence.^{35,36} However, in MBI, maximum compression is characterized by a highly dense but low-temperature proton core.³¹ Conversely, the collapsed bubble in sonoluminescence has a high temperature but relatively low density.

During maximum compression, the number density, n , as a function of r close to the core of the implosion is given by

$$n(r) = \frac{n_0}{6} \left(\frac{R_0}{r} \right)^2, \quad (1)$$

where n_0 is the initial ion density and R_0 is the initial cavity radius.^{31,32} For the case where $n_0 = 5 \times 10^{22}$ cm⁻³, the minimum radius is roughly 0.8 nm.³¹ This suggests that the ions are compressed to 10^5 times that of their original density. This high compression should yield electric fields one order of magnitude lower than the Schwinger limit.³² Hence, vacuum polarization and even pair creation could potentially occur in this scenario.^{33,34} However, it should be noted that Eq. (1) was derived for an infinite quasi-neutral plasma.

Until now, MBI has been investigated under the assumption that the ion distribution is semi-infinite or periodic or when there are multiple laser beams to ensure a sufficient counterflow of electrons. This would confine most of the electrons within the target, leading to a quasi-neutral plasma.

This study addresses the case where the electrons are free to redistribute themselves in the presence of a finite ion distribution after they are given an initial temperature. This implies that the target has a net charge because the electrons can escape to infinity.³⁷ Although some studies have calculated the electron distribution,^{37,38} they assume either the presence of background ion density or the spherical target is solid. This study does not assume the presence of background ions and includes hollow spherical targets.

II. ELECTRON DISTRIBUTION MODEL

To determine the equilibrium electron distribution, Poisson's equation for the electrostatic potential must be solved. It is given as

$$\nabla^2 \phi = 4\pi e(n_e - Zn_i), \quad (2)$$

where e is the elementary charge, Z is the ionization state of the ions, ϕ is the electrostatic potential, and n is the number density. The subscripts e and i denote electrons and ions, respectively. The standard method of solving n_e assumes that the electrons are isothermal and follow the Boltzmann relation, which is expressed as

$$n_e = n_{e0} \exp(e\phi/T), \quad (3)$$

where T is the temperature and n_{e0} is the density as $T \rightarrow \infty$. For spherically symmetric cases, Eqs. (2) and (3) can be solved numerically assuming a static ion distribution. However, the Boltzmann relation is problematic when considering finite-sized targets. As noted by Kanapathipillai *et al.*, for finite-sized spherical targets, it is required that $n_e \rightarrow 0$ as $r \rightarrow \infty$, which implies that $\phi(\infty)$ diverges.³⁸ Hence, the expansion of electrons into a vacuum for finite-sized spherical plasmas should not be isothermal. One solution is to add a small background ion density as this ensures that $\phi(\infty)$ does not diverge and Eq. (3) holds.³⁸

To calculate n_e in a vacuum without the background ions, a more generalized form of Eq. (3) should be used. When the electrons are in hydrostatic equilibrium, an expression for n_e can be obtained by utilizing the polytropic equation of state, $p_e = cn_e^\gamma$, where p is the pressure, γ is the polytropic index, and c is a constant.^{39,40} Thus, n_e can be expressed as

$$n_e = n_{e0} \left(1 + \frac{\gamma - 1}{\gamma} \frac{e\phi}{T_{e0}} \right)^{1/(\gamma-1)}, \quad (4)$$

where the subscript 0 refers to an unperturbed homogeneous plasma (i.e., $n_{e0} = Zn_{i0}$). Unsurprisingly, Eq. (4) is equal to Eq. (3) when considering the isothermal limit ($\gamma \rightarrow 1$). Additionally, $\phi(\infty)$ will not diverge under Eq. (4).

III. ELECTRON DISTRIBUTION FOR A SOLID SPHERE

Using Eqs. (2) and (4), Poisson's equation for the electric potential of a solid sphere with radius R_0 is

$$\frac{\partial^2 \tilde{\phi}}{\partial \xi^2} + \frac{2}{\xi} \frac{\partial \tilde{\phi}}{\partial \xi} = \begin{cases} \Lambda^2 \left(1 + \frac{\gamma - 1}{\gamma} \tilde{\phi} \right)^{1/(\gamma-1)} - \Lambda^2, & \xi \leq 1, \\ \Lambda^2 \left(1 + \frac{\gamma - 1}{\gamma} \tilde{\phi} \right)^{1/(\gamma-1)}, & \xi > 1, \end{cases} \quad (5)$$

where $\xi = r/R_0$, $\tilde{\phi} = e\phi/T$, $\Lambda = R_0/\lambda_{De}$, and λ_{De} is the electron Debye length given by $\sqrt{T_{e0}/(4\pi e^2 n_{e0})}$. Equation (5) can be solved using a finite-difference relaxation algorithm.

In the following calculations, the polytropic index, γ , is 5/3. The electron densities obtained by solving Eq. (5) are compared with three-dimensional molecular dynamics (MD) simulations of electrons. The MD simulations used 10 000 particles, and the ions are modeled as a static uniform cloud of charge. The electrons are initially uniformly distributed in space and given random velocities according to the Maxwell-Boltzmann distribution. The temperatures are calculated

to match the desired Λ . The system is allowed to reach equilibrium, and the time-averaged electron density is calculated.

Figure 1 shows the results of $\tilde{n}_e = n_e/n_{e0}$ from the MD simulations and the numerical solution of Poisson's equation. The results agree well for the different values of Λ . The numerical solution also accurately predicts the known behavior of electrons bound to the ion sphere. As the temperature increases (Λ decreases), the number of electrons bound to the ion sphere decreases. When $\lambda_D = R_0$ ($\Lambda = 1$), only a small fraction of electrons are bound to the ion sphere.

To further quantify this observation, the charge separation, β , of the electrons and ion sphere was calculated and compared with the fitted model described by Peano *et al.*,³⁷ which is given by $\beta = F_{2.6}(2.573/\Lambda)$, where $F_\mu(x) = x/(1+x^\mu)^{1/\mu}$. The charge separation β is the ratio of the total charge of the electrons within the ion sphere to the ion sphere's total charge. This equation was obtained by fitting the $F_\mu(x) = x/(1+x^\mu)^{1/\mu}$ curve to an electron distribution model.³⁷ Our numerical results are almost identical to Peano's fitted model (Fig. 2).

IV. ELECTRON OCCUPANCY IN THE CAVITIES OF HOLLOW SPHERES

For a hollow sphere with an inner radius of R_{in} and an outer radius of R_{out} , Poisson's equation for the electric potential can be written as

$$\frac{\partial^2 \tilde{\phi}}{\partial \xi^2} + \frac{2}{\xi} \frac{\partial \tilde{\phi}}{\partial \xi} = \begin{cases} \Lambda^2 \left(1 + \frac{\gamma - 1}{\gamma} \tilde{\phi} \right)^{1/(\gamma-1)} - \Lambda^2, & 1 \leq \xi \leq \xi_{ar}, \\ \Lambda^2 \left(1 + \frac{\gamma - 1}{\gamma} \tilde{\phi} \right)^{1/(\gamma-1)}, & \text{otherwise,} \end{cases} \quad (6)$$

where $\xi = r/R_{in}$ and $\xi_{ar} = R_{out}/R_{in}$. The second term on the right-hand side, $-\Lambda^2$, corresponds to the ions. It should be noted that all normalizations involving R_0 in Sec. II are replaced with R_{in} in this section.

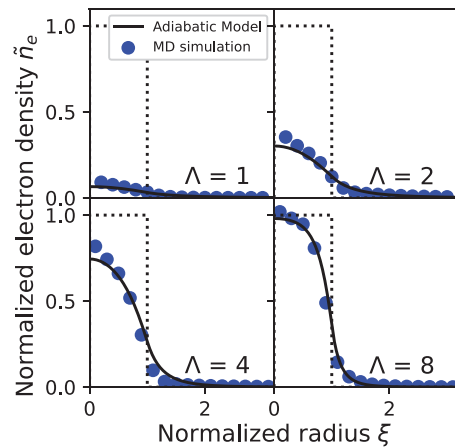


FIG. 1. Calculated normalized electron density profile for the model and MD simulations for different values of Λ .

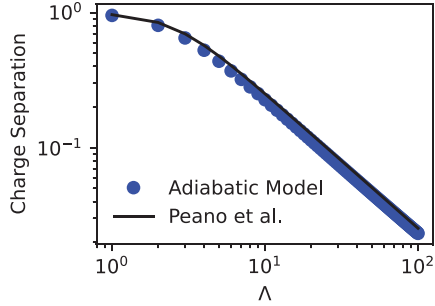


FIG. 2. Calculated charge separation from the numerically solved Poisson's equation and the model derived by Peano et al.³⁷

Figure 3 illustrates the electron density profiles. As λ_{De} of the electrons increases from $R_{in}/8$ to $R_{in}/2$, the number of electrons filling the cavity increases. This is expected because cold electrons are more likely to stay close to the ion sphere. However, increasing λ_{De} past R_{in} decreases the electron distribution because most of the electrons have enough energy to escape the ion sphere completely. This means that, unlike the semi-infinite case where the optimum number of electrons bound in the cavity occurs when $\lambda_{De} \rightarrow \infty$,³¹ finite spheres have an optimum value of Λ where the number of electrons found in the cavity is maximized. Additionally, it can be inferred that the optimum value of Λ depends on $\xi_{ar} = R_{out}/R_{in}$ because as $\xi_{ar} \rightarrow \infty$, $\Lambda \rightarrow 0$ is expected to maximize the number of electrons within the cavity. Therefore, the expression for $\hat{\Lambda}$ can be written as

$$\Lambda_{opt}(\xi_{ar}) = \underset{\Lambda}{\operatorname{argmax}} \int_0^1 n_e(\xi, \Lambda, \xi_{ar}) \xi^2 d\xi, \quad (7)$$

where Λ_{opt} is the optimum value of Λ for a given ξ_{ar} .

Figure 4 shows that as the hollow sphere becomes increasingly thin ($\xi_{ar} \rightarrow 1$), $\Lambda_{opt} \rightarrow \infty$. Additionally, it shows that $\Lambda_{opt} \rightarrow 0$ for

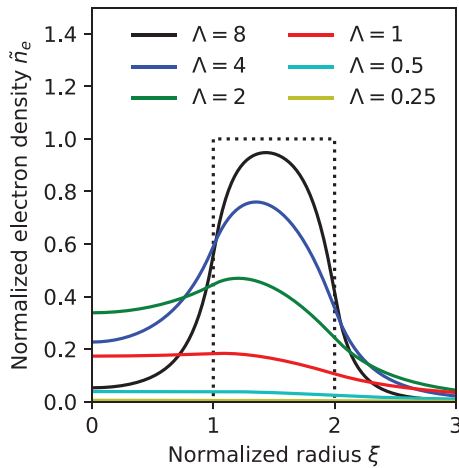


FIG. 3. Electron density profile of a hollow target for various values of Λ . Dotted line denotes the ion density profile.

$\xi_{ar} \rightarrow \infty$. The numerically calculated values for Eq. (7) agree well with the power-law fit $\Lambda_{opt} = 2.875(\xi - 1)^{-0.5257}$. Additionally, as the targets become thicker, the optimum number of electrons within the cavity, $N_e(\xi \leq \xi_{ar})$, also increases. This is an important factor to consider when designing targets for MBI because the compression ratio of MBI depends largely on the number of electrons within the cavity. Although thinner targets require lower electron temperatures to optimally fill the cavity with electrons, there are fewer electrons within the cavity. This trade-off must be considered when designing spherical MBI targets.

V. MBI SIMULATIONS

Because our current model does not diverge as $r \rightarrow \infty$, it can be utilized to simulate the dynamics of a finite MBI target. To simulate the MBI dynamics of a finite spherical shell, a hybrid one-dimensional spherically symmetric molecular dynamics code was implemented. Similar to previous works,^{13,41,42} each simulation particle was assumed to be a spherical shell. This simulation method was investigated in detail and showed to reproduce accurate results on the average.⁴³ However, this simulation model can vary from the single-case results for nano-sized targets. Nevertheless, we expect that these variations will reduce with the increase in the target size.

The protons were treated as spherical shells while the electron density was calculated using the electron model discussed previously. The trajectory of each particle was solved following the equation of motion, which is given by

$$\frac{dp_i}{dt} = \sum_{r_j < r_i} \frac{Q_i Q_j}{r_j^2} + \frac{Q_i^2}{2r_i^2} + Q_i E(r_i), \quad (8)$$

where the simulation particles' charge, momentum, and radius are expressed as Q , p , and r , respectively. $E(r)$ is the electric field of the electrons, which can be obtained by solving Eqs. (2) and (4). Using this model to calculate the electron density and treating the protons as simulation particles, the overall accuracy of the simulation

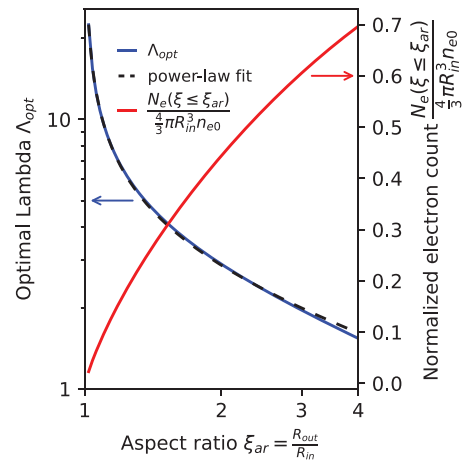


FIG. 4. Numerically calculated Λ_{opt} as a function of ξ_{ar} , along with the power-law fit and the normalized number of electrons within the cavity.

can be maintained while reducing the total number of simulation particles needed because particles to simulate the electrons are not necessary.

For the simulation parameters, the targets were assumed to be composed of pure hydrogen. The default electron temperatures were set to be the optimum temperature as defined by Eq. (7). For all simulations, the cavity's radius was set to $1\text{ }\mu\text{m}$, and the initial density was set to $n_i = 5 \times 10^{22}\text{ cm}^{-3}$. Additionally, for ideal MBI, when the initial density and bubble radius is $5 \times 10^{22}\text{ cm}^{-3}$ and $1\text{ }\mu\text{m}$, respectively, the bubble will be compressed to a minimum radius of 0.8 nm with a corresponding compression rate of $\sim 10^5$.

A. Simulation results

Figure 5 shows the trajectories of the MBI simulations. Indeed, MBI occurs even for a finite hollow sphere. Furthermore, all three cases considered in Fig. 5 indicate proton flashing. Unlike the typical MBI results for semi-infinite geometries, in these cases, charge separation resulting from high electron temperatures causes the outer layer to expand. Along with the flashed ions from the imploding inner layer, the expanding outer layer is also a source of accelerated ions. As the thickness of the hollow sphere increases, the implosion time decreases (Fig. 5).

MBI is a process that relies heavily on the number of electrons contained within the cavity. As the aspect ratio increases, the maximum number of electrons that can be contained within the cavity also increases (Fig. 4). More electrons present within the cavity should increase the implosion velocity of the ions, implying a shorter implosion time.³¹

All three cases considered can achieve a density compression ratio of 10^4 times that of the solid density (Fig. 6). This is one order of magnitude lower from the 10^5 compression ratio predicted using an ideal semi-infinite system given by Eq. (1). Nevertheless, Fig. 6 illustrates that high compression ratios are possible even with a finite target. More importantly, as the aspect ratio increases, the agreement

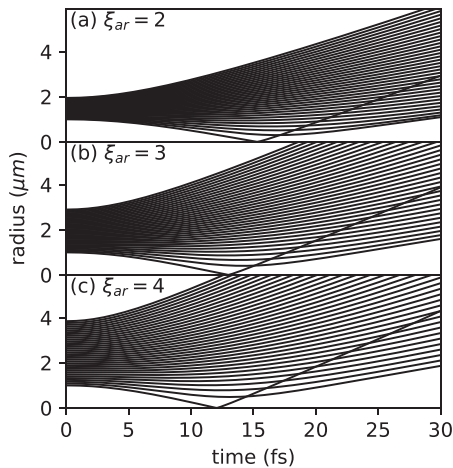


FIG. 5. Trajectory of a hollow sphere with $1\text{-}\mu\text{m}$ cavity undergoing MBI for different aspect ratios: (a) $\xi_{ar} = 2$, (b) $\xi_{ar} = 3$, and (c) $\xi_{ar} = 4$.

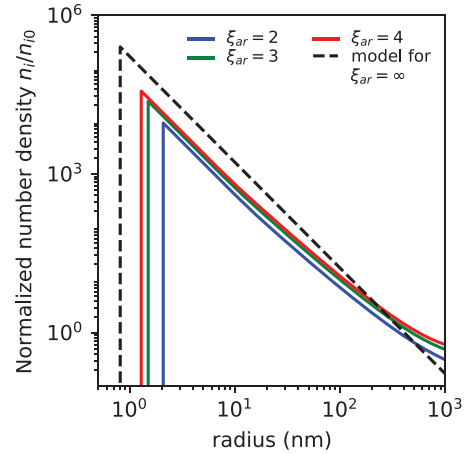


FIG. 6. Density profile during maximum compression of a hollow sphere with $1\text{-}\mu\text{m}$ cavity undergoing MBI for different aspect ratios. The dashed line is the model given by Eq. (1).

between the density profile and the theoretical model given by Eq. (1) improves.

The energy distribution plots show evidence of ion flashing described by earlier studies^{31,32} (Fig. 7). Comparisons confirm that the small spikes in the graphs agree well with the energies of the inner layers. This implies that these spikes are due to the flashing of the inner ion layers. An interesting observation is that most of the flashed ion layers have lower energies than the outermost Coulomb exploding layer. Hence, it is difficult to distinguish the flashed layers from the normal Coulomb exploding layer. However, for $\xi_{ar} = 2$, the innermost layer attains an energy of over 600 MeV , which is higher than the energy of the outermost Coulomb exploding layer. This implies that it would be difficult to detect ion flashing if targets are too thick ($\xi_{ar} > 2$).

According to Fig. 8, targets with $\xi_{ar} > 2.2$ will not produce flashed ions. Λ_{opt} is larger for thicker targets. As Λ_{opt} increases, the charge separation between electrons and ions also increases. This increases the total energy of the Coulomb exploding outer layers. On the other hand, the acceleration of the inner layers is influenced by the total number of electrons in the cavity.^{31,32} According to Fig. 4, thinner targets have less electrons. This implies that if the target is too thin, the proton flashing is minimal. Figure 8 shows that when $\xi_{ar} < 1.3$, the energy ratio starts to decrease. Therefore, to maximize proton flashing, the target should have $\xi_{ar} = 1.3$.

VI. SUMMARY AND CONCLUSION

Using the model described by Eq. (6), a one-dimensional hybrid code was developed to simulate MBI for finite spheres. MBI occurs for finite spheres. The density compression ratio for the cases studied is $\sim 10^4$. For hollow spherical targets with the same cavity radius, thicker targets produce a higher density compression. However, observing ion flashing is more difficult in thicker targets because the Coulomb exploding outer layers have much higher energies.

Nevertheless, finite hollow spherical targets are indeed viable for MBI even without containing the electrons within the target.

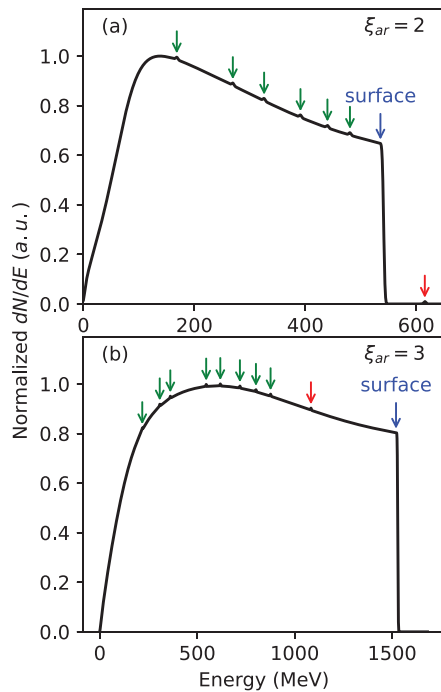


FIG. 7. Energy distribution of a hollow sphere with $1\text{-}\mu\text{m}$ cavity undergoing MBI for (a) $\xi_{ar} = 2$ and (b) $\xi_{ar} = 3$. Green arrows indicate flashed ions, the red arrow indicates the innermost layer, and the blue arrow indicates the surface layer.

This implies that proof-of-principle experiments can be conducted on finite targets by providing the electrons an initial temperature and allowing the natural time evolution of the system to proceed. This may reduce the complexity required to conduct proof-of-principle experiments about MBI. It should be noted that the target's aspect ratio plays an important role in the different applications of MBI. As we have observed, targets with high aspect ratios should have better compression ratios. Unfortunately, ion flashing in high aspect ratio targets is difficult to detect because the outer layers attain large energies during

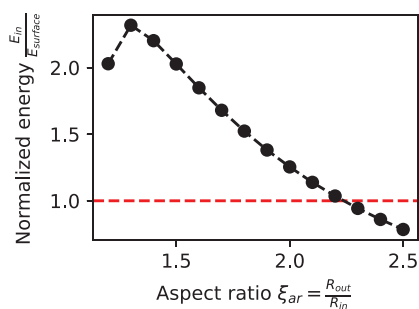


FIG. 8. The ratio of the innermost ion energy, E_{im} , to the surface ion energy, $E_{surface}$, vs ξ_{ar} .

a Coulomb explosion. Targets with large aspect ratios tend to require more laser energy because their optimal Λ is much lower. Although creating a dense core is essential for gamma-ray lensing and pair creation, ion flashing is the essence of ion acceleration applications for MBI. As long as $\xi_{ar} < 2.2$ and Λ_{opt} is used, there will be flashed ions. Consequently, finite MBI targets should be tailored to the specific application to be observed.

ACKNOWLEDGMENTS

M. Murakami was supported by the Japan Society for the Promotion of Science (JSPS). M. A. H. Zosa thanks Y. Gu and D. Shokov for fruitful discussions.

AUTHOR DECLARATIONS

Conflict of Interest

The authors have no conflicts to disclose.

DATA AVAILABILITY

The data that support the findings of this study are available from the corresponding author upon reasonable request.

REFERENCES

- ¹J. W. Yoon, Y. G. Kim, I. W. Choi, J. H. Sung, H. W. Lee, S. K. Lee, and C. H. Nam, "Realization of laser intensity over 10^{23} W/cm^2 ," *Optica* **8**, 630 (2021).
- ²Z. Zhang, F. Wu, J. Hu, X. Yang, J. Gui, P. Ji, X. Liu, C. Wang, Y. Liu, X. Lu, Y. Xu, Y. Leng, R. Li, and Z. Xu, "The laser beamline in SULF facility," *High Power Laser Sci. Eng.* **8**, e4 (2020).
- ³C. A. Haynam, P. J. Wegner, J. M. Auerbach, M. W. Bowers, S. N. Dixit, G. V. Erbert, G. M. Heestand, M. A. Hennesian, M. R. Hermann, K. S. Jancaitis, K. R. Manes, C. D. Marshall, N. C. Mehta, J. Menapace, E. Moses, J. R. Murray, M. C. Nostrand, C. D. Orth, R. Patterson, R. A. Sacks, M. J. Shaw, M. Spaeth, S. B. Sutton, W. H. Williams, C. C. Widmayer, R. K. White, S. T. Yang, and B. M. V. Wouterghem, "National Ignition Facility laser performance status," *Appl. Opt.* **46**, 3276 (2007).
- ⁴H. Shiraga, S. Fujioka, M. Nakai, T. Watari, H. Nakamura, Y. Arikawa, H. Hosoda, T. Nagai, M. Koga, H. Kikuchi, Y. Ishii, T. Sogo, K. Shigemori, H. Nishimura, Z. Zhang, M. Tanabe, S. Ohira, Y. Fujii, T. Namimoto, Y. Sakawa, O. Maegawa, T. Ozaki, K. Tanaka, H. Habara, T. Iwawaki, K. Shimada, H. Nagatomo, T. Johzaki, A. Sunahara, M. Murakami, H. Sakagami, T. Taguchi, T. Norimatsu, H. Homma, Y. Fujimoto, A. Iwamoto, N. Miyanaga, J. Kawanaka, T. Jitsuno, Y. Nakata, K. Tsubakimoto, N. Morio, T. Kawasaki, K. Sawai, K. Tsuji, H. Murakami, T. Kanabe, K. Kondo, N. Sarukura, T. Shimizu, K. Mima, and H. Azechi, "Fast ignition integrated experiments with Gekko and LFEX lasers," *Plasma Phys. Controlled Fusion* **53**, 124029 (2011).
- ⁵L. Torrisi, "Ion energy enhancement from TNSA plasmas obtained from advanced targets," *Laser Part. Beams* **32**, 383–389 (2014).
- ⁶A. Macchi, S. Veghini, T. V. Liseykina, and F. Pegoraro, "Radiation pressure acceleration of ultrathin foils," *New J. Phys.* **12**, 045013 (2010).
- ⁷A. Henig, S. Steinke, M. Schnürer, T. Sokollik, R. Hörlein, D. Kiefer, D. Jung, J. Schreiber, B. M. Hegelich, X. Q. Yan, J. M. ter Vehn, T. Tajima, P. V. Nickles, W. Sandner, and D. Habs, "Radiation-pressure acceleration of ion beams driven by circularly polarized laser pulses," *Phys. Rev. Lett.* **103**, 245003 (2009).
- ⁸S. S. Bulanov, A. Brantov, V. Y. Bychenkov, V. Chvykov, G. Kalinchenko, T. Matsuoka, P. Rousseau, S. Reed, V. Yanovsky, D. W. Litzenberg, K. Krushelnick, and A. Maksimchuk, "Accelerating monoenergetic protons from ultrathin foils by flat-top laser pulses in the directed-Coulomb-explosion regime," *Phys. Rev. E* **78**, 026412 (2008).
- ⁹T. Z. Esirkepov, Y. Sentoku, K. Mima, K. Nishihara, F. Califano, F. Pegoraro, N. M. Naumova, S. V. Bulanov, Y. Ueshima, T. V. Liseykina, V. A. Vshivkov, and Y. Kato, "Ion acceleration by superintense laser pulses in plasmas," *J. Exp. Theor. Phys. Lett.* **70**, 82–89 (1999).

- ¹⁰J. Jortner and I. Last, "Ultrafast nuclear dynamics and non-uniform Coulomb explosion of heteroclusters," *Mol. Phys.* **103**, 1735–1743 (2005).
- ¹¹I. Last and J. Jortner, "Ultrafast high-energy dynamics of thin spherical shells of light ions in the Coulomb explosion of heteroclusters," *Phys. Rev. A* **71**, 063204 (2005).
- ¹²S. C. Wilks, A. B. Langdon, T. E. Cowan, M. Roth, M. Singh, S. Hatchett, M. H. Key, D. Pennington, A. MacKinnon, and R. A. Snavely, "Energetic proton generation in ultra-intense laser–solid interactions," *Phys. Plasmas* **8**, 542–549 (2001).
- ¹³E. Boella, B. P. Paradisi, A. D'Angola, L. O. Silva, and G. Coppa, "Study on Coulomb explosions of ion mixtures," *J. Plasma Phys.* **82**, 905820110 (2016).
- ¹⁴W. Lu, M. Tzoufras, C. Joshi, F. S. Tsung, W. B. Mori, J. Vieira, R. A. Fonseca, and L. O. Silva, "Generating multi-GeV electron bunches using single stage laser wakefield acceleration in a 3D nonlinear regime," *Phys. Rev. Spec. Top. Accel. Beams* **10**, 061301 (2007).
- ¹⁵R. Wagner, S.-Y. Chen, A. Maksimchuk, and D. Umstadter, "Electron acceleration by a laser wakefield in a relativistically self-guided channel," *Phys. Rev. Lett.* **78**, 3125–3128 (1997).
- ¹⁶A. V. Arefiev, V. N. Khudik, and M. Schollmeier, "Enhancement of laser-driven electron acceleration in an ion channel," *Phys. Plasmas* **21**, 033104 (2014).
- ¹⁷W. Yu, V. Bychenkov, Y. Sentoku, M. Y. Yu, Z. M. Sheng, and K. Mima, "Electron acceleration by a short relativistic laser pulse at the front of solid targets," *Phys. Rev. Lett.* **85**, 570–573 (2000).
- ¹⁸A. Buck, M. Nicolai, K. Schmid, C. M. S. Sears, A. Sävert, J. M. Mikhailova, F. Krausz, M. C. Kaluza, and L. Veisz, "Real-time observation of laser-driven electron acceleration," *Nat. Phys.* **7**, 543–548 (2011).
- ¹⁹M. Murakami, "Irradiation system based on dodecahedron for inertial confinement fusion," *Appl. Phys. Lett.* **66**, 1587–1589 (1995).
- ²⁰M. Murakami and D. Nishi, "Optimization of laser illumination configuration for directly driven inertial confinement fusion," *Matter Radiat. Extremes* **2**, 55–68 (2017).
- ²¹R. Betti and O. A. Hurricane, "Inertial-confinement fusion with lasers," *Nat. Phys.* **12**, 435–448 (2016).
- ²²H.-S. Park, O. Hurricane, D. Callahan, D. Casey, E. Dewald, T. Dittrich, T. Döppner, D. Hinkel, L. B. Hopkins, S. L. Pape, T. Ma, P. Patel, B. Remington, H. Robey, J. Salmonson, and J. Kline, "High-adiabat high-foot inertial confinement fusion implosion experiments on the National Ignition Facility," *Phys. Rev. Lett.* **112**, 055001 (2014).
- ²³J. E. Ralph, O. Landen, L. Divol, A. Pak, T. Ma, D. A. Callahan, A. L. Kritcher, T. Döppner, D. E. Hinkel, C. Jarrott, J. D. Moody, B. B. Pollock, O. Hurricane, and M. J. Edwards, "The influence of hohlraum dynamics on implosion symmetry in indirect drive inertial confinement fusion experiments," *Phys. Plasmas* **25**, 082701 (2018).
- ²⁴D. L. Burke, R. C. Field, G. Horton-Smith, J. E. Spencer, D. Walz, S. C. Berridge, W. M. Bugg, K. Shmakov, A. W. Weidemann, C. Bula, K. T. McDonald, E. J. Prebys, C. Bamber, S. J. Boege, T. Koffas, T. Kotseroglou, A. C. Melissinos, D. D. Meyerhofer, D. A. Reis, and W. Ragg, "Positron production in multiphoton light-by-light scattering," *Phys. Rev. Lett.* **79**, 1626–1629 (1997).
- ²⁵A. Titov, H. Takabe, and B. Kämpfer, "Nonlinear breit-wheeler process in short laser double pulses," *Phys. Rev. D* **98**, 036022 (2018).
- ²⁶K. Krajewska and J. Z. Kamiński, "Breit-Wheeler process in intense short laser pulses," *Phys. Rev. A* **86**, 052104 (2012).
- ²⁷M. Vranic, O. Klimo, G. Korn, and S. Weber, "Multi-GeV electron-positron beam generation from laser-electron scattering," *Sci. Rep.* **8**, 4702 (2018).
- ²⁸Y.-J. Gu, O. Klimo, S. V. Bulanov, and S. Weber, "Brilliant gamma-ray beam and electron–positron pair production by enhanced attosecond pulses," *Commun. Phys.* **1**, 93 (2018).
- ²⁹Y.-J. Gu and S. Weber, "Intense, directional and tunable γ -ray emission via relativistic oscillating plasma mirror," *Opt. Express* **26**, 19932 (2018).
- ³⁰Y.-J. Gu, M. Jirka, O. Klimo, and S. Weber, "Gamma photons and electron-positron pairs from ultra-intense laser-matter interaction: A comparative study of proposed configurations," *Matter Radiat. Extremes* **4**, 064403 (2019).
- ³¹M. Murakami, A. Arefiev, and M. A. Zosa, "Generation of ultrahigh field by micro-bubble implosion," *Sci. Rep.* **8**, 7537 (2018).
- ³²M. Murakami, A. Arefiev, M. A. Zosa, J. K. Koga, and Y. Nakamiya, "Relativistic proton emission from ultrahigh-energy-density nanosphere generated by microbubble implosion," *Phys. Plasmas* **26**, 043112 (2019).
- ³³J. K. Koga, M. Murakami, A. V. Arefiev, and Y. Nakamiya, "Probing and possible application of the QED vacuum with micro-bubble implosions induced by ultra-intense laser pulses," *Matter Radiat. Extremes* **4**, 034401 (2019).
- ³⁴J. K. Koga, M. Murakami, A. V. Arefiev, Y. Nakamiya, S. S. Bulanov, and S. V. Bulanov, "Electron-positron pair creation in the electric fields generated by micro-bubble implosions," *Phys. Lett. A* **384**, 126854 (2020).
- ³⁵L. Rayleigh, "VIII. On the pressure developed in a liquid during the collapse of a spherical cavity," *London, Edinburgh, Dublin Philos. Mag. J. Sci.* **34**, 94–98 (1917).
- ³⁶B. P. Barber and S. J. Putterman, "Light scattering measurements of the repetitive supersonic implosion of a sonoluminescing bubble," *Phys. Rev. Lett.* **69**, 3839–3842 (1992).
- ³⁷F. Peano, J. L. Martins, R. A. Fonseca, L. O. Silva, G. Coppa, F. Peinetti, and R. Mulas, "Dynamics and control of the expansion of finite-size plasmas produced in ultraintense laser-matter interactions," *Phys. Plasmas* **14**, 056704 (2007).
- ³⁸M. Kanopathipillai, P. Mulser, D. H. H. Hoffmann, T. Schlegel, Y. Maron, and R. Sauerbrey, "Net charge of a conducting microsphere embedded in a thermal plasma," *Phys. Plasmas* **11**, 3911–3914 (2004).
- ³⁹C. Sack and H. Schamel, "Plasma expansion into vacuum—A hydrodynamic approach," *Phys. Rep.* **156**, 311–395 (1987).
- ⁴⁰G. Manfredi, S. Mola, and M. R. Feix, "Rescaling methods and plasma expansions into vacuum," *Phys. Fluids B* **5**, 388–401 (1993).
- ⁴¹M. A. H. Zosa and M. Murakami, "Generation of quasi-monoenergetic ions using optimized hollow nanospheres," *Phys. Plasmas* **27**, 033103 (2020).
- ⁴²M. Murakami and K. Mima, "Efficient generation of quasimonoenergetic ions by Coulomb explosions of optimized nanostructured clusters," *Phys. Plasmas* **16**, 103108 (2009).
- ⁴³A. D'Angola, E. Boella, and G. Coppa, "On the applicability of the standard kinetic theory to the study of nanoplasmas," *Phys. Plasmas* **21**, 082116 (2014).